Article

Microstructure and Hydrogen Storage Properties of the Multiphase $Ti_{0.3}V_{0.3}Mn_{0.2}Fe_{0.1}Ni_{0.1}$ Alloy

Salma Sleiman, Maria Moussa and Jacques Huot *

Hydrogen Research Institute, Université du Québec à Trois-Rivières, 3351 des Forges, Trois-Rivières, QC G9A 5H7, Canada; salma.sleiman@irh.ca (S.S.); maria.moussa@irh.ca (M.M.)
* Correspondence: jacques.huot@irh.ca; Tel.: +1-819-376-5011 (ext. 3576)

Abstract: The hydrogen storage properties of a multi-component alloy of composition $Ti_{0.3}V_{0.3}Mn_{0.2}Fe_{0.1}Ni_{0.1}$ were investigated. The alloy was synthesized by arc melting and mechanical alloying, resulting in different microstructures. It was found that the as-cast alloy is multiphase, with a main C14 Laves phase matrix along with a BCC phase and a small amount of Ti_2Fe-type phase. The maximum hydrogen storage capacity of the alloy was 1.6 wt.%. We found that the air-exposed samples had the same capacity as the as-cast sample but with a longer incubation time. Synthesis by mechanical alloying for five hours resulted in an alloy with only BCC structure. The hydrogen capacity of the milled alloy was 1.2 wt.%, lower than the as-cast one. The effect of ball milling of the as-cast alloy was also studied. Ball milling for five hours produced a BCC structure similar to the one obtained by milling the raw materials for the same time.

Keywords: hydrogen storage; C14 Laves phase; mechanical alloying; kinetics

1. Introduction

Hydrogen is considered an attractive energy vector for renewable energies. However, its storage in a safe, compact, and inexpensive way is still an important issue. A variety of hydrogen storage systems are possible: liquid, compressed gas, physisorption on high specific surface area materials, and metal hydrides [1–3]. Among these techniques, metal hydrides in which hydrogen forms a chemical bond with the metal atoms are attractive due to the high volumetric density and moderate operation conditions [4].

In 2004, Cantor et al. [5] and Yeh et al. [6] independently proposed the concept of high entropy alloys (HEAs). HEAs are an advanced type of multi-component alloy system [7]. The definition of HEAs is usually based on composition or configurational entropy. From the composition-based definition, HEAs contain at least five principal elements, each with an atomic abundance between 5 and 35%. Based on entropy, HEAs are alloys having configurational entropies greater than or equal to 1.5 R, where R is the gas constant. An alloy fitting one of these two definitions could be considered a HEA. However, these definitions should be considered guidelines and not laws. Because of the nature of HEAs, they have interesting properties such as high thermal stability, good ductility, high strength, good corrosion resistance, etc., [8].

Recently, HEAs have been considered for hydrogen storage [9–12]. Kunce et al. studied the high entropy alloy ZrTiVCrFeNi prepared by laser engineered net shaping (LENS). This alloy was mainly C14 Laves phase with small amount of α-Ti phase. After heat treatment at 500 °C, the maximum hydrogen capacity was found to be 1.8 wt.% under 100 bars of hydrogen at 50 °C. Additional heat treatment at 1000 °C had no effect on the crystal structure but reduced the capacity to 1.56 wt.% under the same absorption conditions [9]. Kunce et al. also examined another high entropy alloy TiZrNbMoV [10]. Depending on LENS synthesis conditions, this alloy exhibited different phase compositions. The predominant BCC TiZrNbMoV alloy absorbed only 0.59 wt.% under 85 bar at 50 °C without prior heat treatment [10]. However, the multiphase alloy prepared with a higher laser

power absorbed 2.3 wt.% of hydrogen in less than 25 min under the same hydrogenation conditions [10]. Sahlberg et al. investigated the alloy TiZrHfNbV and found that it could absorb 2.7 wt.% of hydrogen at 300 °C [12]. They pointed out that hydrogen desorbed completely at 500 °C under vacuum [13]. Kao et al. prepared by arc melting $CoFeMnTi_xV_yZr_z$ alloys which have a single C14 Laves phase. The maximum capacity was 1.8 wt.% at room temperature with prior heat treatment at 400 °C [14]. Zepon et al. synthesized by high energy ball milling a nanocrystalline $MgZrTiFe_{0.5}Co_{0.5}Ni_{0.5}$ HEA with a single BCC phase. This BCC alloy absorbed 1.2 wt.% at 350 °C under 20 bars of hydrogen [15]. These results indicate that HEAs have interesting hydrogen storage properties.

In the present work, the transition elements of period 4, Ti, V, Mn, Fe, and Ni, were selected. They are not all strong hydride forming elements, but not using the heavier elements of periods 5 or 6 means that the gravimetric hydrogen storage capacity may be higher. The composition was selected by taking into account the thermodynamic, geometric, and electronic parameters.

The phase formation is thermodynamically controlled by the Gibbs free energy ΔG. ΔG can be determined by Equation (1):

$$\Delta G_{mix} = \Delta H_{mix} - T\Delta S_{mix}, \tag{1}$$

where ΔH_{mix} is the enthalpy of mixing, ΔS_{mix} is the entropy of mixing of the alloys and T is the absolute temperature. ΔS_{mix} and ΔH_{mix} are calculated according to Formulas (2) and (3), respectively [6,16]:

$$\Delta S_{mix} = -R\sum_{i=1}^{N} C_i \ln C_i, \tag{2}$$

where R is the gas constant (8.314 J·mol^{-1}·K^{-1}), N is the number of elements of the alloy, and C_i is the percentage of each element of the alloy.

$$\Delta H_{mix} = \sum_{i=1,i\neq j}^{N} 4\Delta H_{AB}^{mix} C_i C_j, \tag{3}$$

where ΔH_{AB}^{mix} is the binary enthalpy of equiatomic AB alloy taken from [17].

Yang and Zhang proposed a dimensionless parameter Ω that combines the effects of ΔS_{mix} and ΔH_{mix} [18]. Ω is defined as:

$$\Omega = \frac{T_m \Delta S_{mix}}{|\Delta H_{mix}|}, \tag{4}$$

where T_m is the melting temperature of the alloy determined by the rule of mixtures:

$$T_m = \sum_{i=1}^{N} C_i (T_m)_i, \tag{5}$$

where $(T_m)_i$ is the melting temperature of the ith element.

The geometric parameter is characterized by the atomic size difference δ of the constituent elements. δ is calculated using the following relation [19]:

$$\delta\% = 100\%\sqrt{\sum_{i=1}^{N} C_i \left(1 - \frac{r_i}{\sum_{i=1}^{N} C_i r_i}\right)^2}, \tag{6}$$

where r_i is the atomic radius of element i.

Empirically, it was found that when $\Omega \geq 1.1$ and $\delta \leq 6.6\%$, the formation of solid solution phases are suggested [18].

The electronic parameter is the valence electron concentration (VEC) of the constituent elements. VEC predicts the phase selection between FCC and BCC type solid solutions [20]. It is given by Equation (7):

$$\text{VEC} = \sum_{i=1}^{N} C_i (VEC)_i, \tag{7}$$

where $(VEC)_i$ is the VEC for the ith element, which is the number of total electrons in the valence band including d electrons. The VECs of for Ti, V, Mn, Fe, and Ni are, respectively 4, 5, 7, 8, and 10. A value of VEC smaller than 6.87 means that BCC phase formation is favored over FCC [20].

Based on the criteria Ω, δ, and VEC, we selected the composition $Ti_{0.3}V_{0.3}Mn_{0.2}Fe_{0.1}Ni_{0.1}$. For this composition, ΔH_{mix} is equal to -12.84 kJ·mol^{-1} and ΔS_{mix} is 12.51 J·K^{-1}mol^{-1}, giving $\Omega = 1.84$. δ was calculated to be 5.4% using the atomic radii taken from [21]. VEC value was found to be 5.9 (data taken from [22]), which means that the BCC phase is most likely to occur. The aim of this investigation was to study the crystal structure and hydrogen storage properties of $Ti_{0.3}V_{0.3}Mn_{0.2}Fe_{0.1}Ni_{0.1}$ alloy synthesized by arc melting and ball milling. The effect of ball milling the as-cast alloy was also examined.

2. Materials and Methods

All raw materials, Ti sponge (99.9%), V pieces (99.9%), Mn chunks (99.9%), Fe pieces (99.9%), and Ni pieces (99%) were purchased from Alfa Aesar. The $Ti_{0.3}V_{0.3}Mn_{0.2}Fe_{0.1}Ni_{0.1}$ alloys were prepared by arc melting and by mechanical alloying after mixing all raw elements at the desired proportions. The subscripts mean the mole fractions of the constituent elements. The melting was done under 0.7 bars of argon. Each pellet was melted, turned over, and remelted three times to ensure good homogeneity. The as-cast alloys were hand-crushed using a hardened steel mortar and pestle. Ball milling was carried out on a SPEX high energy mill 8000 M in a hardened steel crucible and balls. The ball-to-metal mass ratio was 10 and milling was done for 1, 5, and 10 h. The crucible was loaded in an argon-filled glovebox. The hydrogen sorption properties were measured using a home-made Sievert's apparatus. The powder was filled in a reactor and kept under dynamic vacuum for one hour at room temperature before its exposure to hydrogen. The crystal structure was determined by X-ray powder diffraction using a Bruker D8 Focus with Cu Kα radiation. Crystal structure parameters were evaluated from Rietveld refinement using Topas software [23]. Microstructure and chemical analysis were performed using a Hitachi Su1510 scanning electron microscopy (SEM) equipped with an EDX (energy-dispersive X-ray) apparatus from Oxford Instruments. The relative abundance of each phase was evaluated from micrographs using ImageJ software [24].

3. Results and Discussions

3.1. Microstructural Study

Figure 1 shows the backscattered electron micrograph of as-cast $Ti_{0.3}V_{0.3}Mn_{0.2}Fe_{0.1}Ni_{0.1}$ alloy.

The different shades of grey indicate a multiphase alloy. Using ImageJ, the area percentages for the bright, grey, and dark grey phases were found to be, respectively 66%, 25%, and 9%. Being the dominant phase, the bright phase is thereafter called "matrix".

The chemical composition of the alloy was determined by EDX measurement. Table 1 shows the bulk measured atomic abundance compared to the nominal composition. We see that the bulk measured composition agrees with the nominal one.
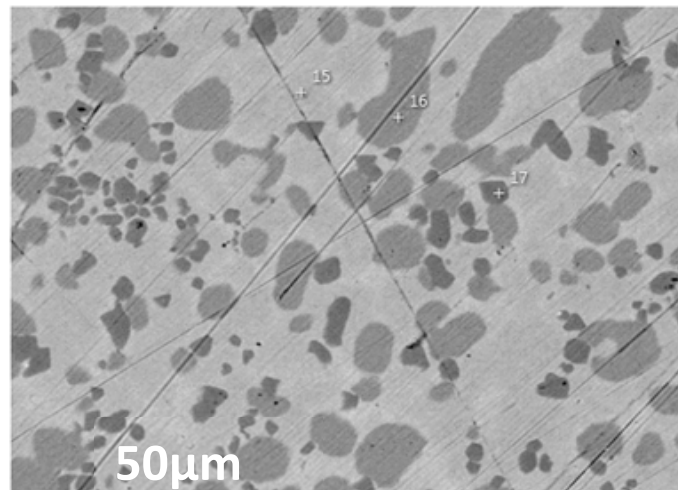
Figure 1. Backscattered electron (BSE) micrograph of as-cast $Ti_{0.3}V_{0.3}Mn_{0.2}Fe_{0.1}Ni_{0.1}$ alloy.

Table 1. Bulk atomic abundance: nominal and as measured by EDX of as-cast $Ti_{0.3}V_{0.3}Mn_{0.2}Fe_{0.1}Ni_{0.1}$ alloy. Error on the last significant digit is indicated in parentheses.

Element (at.%)	Ti	V	Mn	Fe	Ni
Nominal	30	30	20	10	10
Measured	29.4 (3)	30.8 (1)	19.1 (2)	10.4 (1)	10.3 (2)

Using EDX, we also measured the chemical composition of each phase. The EDX point analysis was performed at a higher magnification on the regions presented in Figure 2.
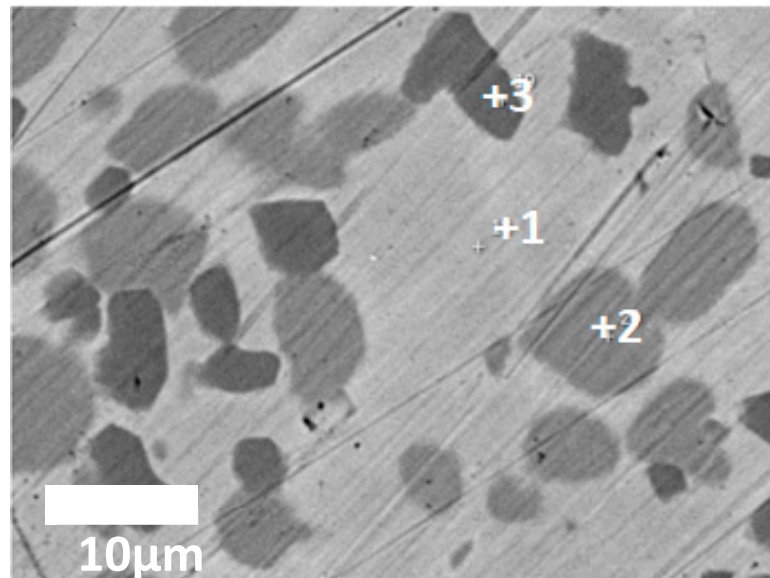
Figure 2. BSE micrograph of as-cast $Ti_{0.3}V_{0.3}Mn_{0.2}Fe_{0.1}Ni_{0.1}$ alloy.

In this micrograph, the matrix, grey, and dark grey phases are indicated by points number 1, 2, and 3, respectively. Their chemical composition is listed in Table 2.

Table 2. EDX analysis showing the elemental composition of all the phases of as-cast $Ti_{0.3}V_{0.3}Mn_{0.2}Fe_{0.1}Ni_{0.1}$ alloy. Error on all values is 1 at.%.

Element (at.%)	Ti	V	Mn	Fe	Ni
Matrix (Point 1)	32	23	19	11	15
Grey phase (Point 2)	16	51	21	9	3
Dark grey (Point 3)	51	13	11	11	14

The matrix is relatively close to the nominal composition, only slightly depleted in vanadium and rich in nickel. The major constituent of the grey phase is vanadium while titanium is the main element in the dark grey phase. Nickel and iron are mainly in the matrix and dark grey phase. Iron is uniformly distributed over all phases.

3.2. Crystal Structure

Figure 3 presents the XRD patterns of $Ti_{0.3}V_{0.3}Mn_{0.2}Fe_{0.1}Ni_{0.1}$ alloy in as-cast state. The following phases were found to give the best Rietveld refinement fit for this pattern: C14 Laves phase (space group *P6₃/mmc*, structure type $MgZn_2$), BCC phase (space group *Im-3m*, structure type W), and Ti_2Fe type phase (space group Fd-3m:2, structure type Ti_2Ni). The lattice parameters and the abundance of these phases are presented in Table 3.
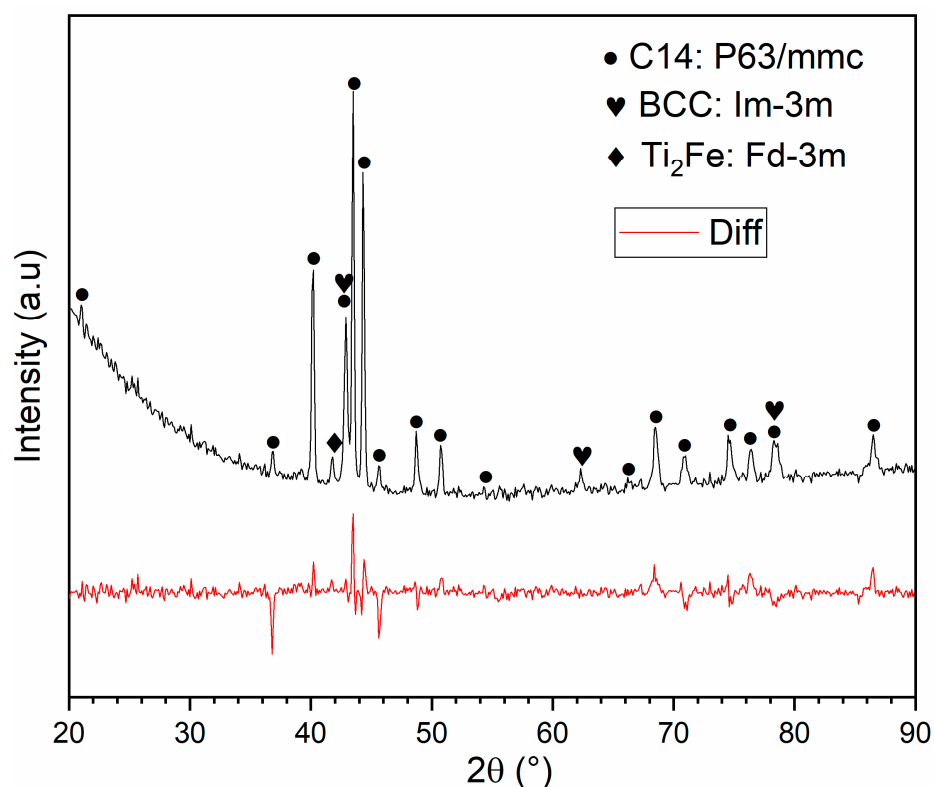
Figure 3. X-ray diffraction patterns of as-cast $Ti_{0.3}V_{0.3}Mn_{0.2}Fe_{0.1}Ni_{0.1}$ alloy. The bottom curve is the difference between calculated and measured intensities.

Table 3. Crystal parameters and abundance of each phase of as-cast $Ti_{0.3}V_{0.3}Mn_{0.2}Fe_{0.1}Ni_{0.1}$ alloy. Error on the last significant digit is indicated in parentheses.

Phase	Unit Cell Volume Å³	Lattice Parameter Å	Crystallite Size nm	Micro-Strain %	Abundance %
C14	164.98 (3)	a = 4.8900 (4) c = 7.9651 (9)	125 (48)	0.04 (1)	79
BCC	26.58 (1)	2.9841 (5)	31 (5)	——	17
Ti_2Fe	1418 (3)	11.234 (8)	——	——	4

Correlating the abundance of the phases as measured by ImageJ software with the percentage of phases as determined by Rietveld's analysis, we see that the C14 phase may be associated with the matrix. From Table 2, the matrix composition could be written $Ti_{0.96}V_{0.69}Mn_{0.57}Fe_{0.33}Ni_{0.45}$. For the relatively close composition $Ti_1V_{0.64}Mn_{0.81}Fe_{0.15}Ni_{0.4}$, Song et al. found that the crystal structure was C14 [25]. Therefore, it is reasonable to associate the C14 crystal structure with the matrix phase. In their analysis, Song et al. assigned Ti to the *4f* site and the other atoms were evenly distributed on the other two sites (*2a* and *6h*) [25]. From the chemical composition of the matrix presented in Table 2, we see that the same assignation could be done here.

The abundance of the BCC phase roughly matches the abundance of the grey phase. Again, using Table 2 we could assume that the BCC phase has a composition of $Ti_{0.16}V_{0.51}Mn_{0.21}Fe_{0.09}Ni_{0.03}$. This is supported by the fact that there is a wide range of $Ti_{1-x-y}V_xMn_y$ that has the BCC structure [26–34]. The least abundant phase (dark grey) has a composition that could be written as $Ti_{1.53}V_{0.39}Mn_{0.33}Fe_{0.33}Ni_{0.42}$. The diffraction pattern indicates the presence of a Ti_2Fe-like phase, which roughly matches the abundance of the dark grey phase. As Ti_2Ni is the structure type of Ti_2Fe, it is reasonable to assume that the dark grey phase has the Ti_2Fe structure with vanadium most likely substituted for Ti and Mn substituting for Ni/Fe.

According to the criteria used for Ω, δ, and VEC, the as-cast $Ti_{0.3}V_{0.3}Mn_{0.2}Fe_{0.1}Ni_{0.1}$ alloy should adopt a BCC phase. However, the main phase found is the C14 phase instead of BCC. One can see that Ω is 1.84 higher than the condition proposed by Yang and Zhang [18]. However, the absolute of ΔH_{mix} (12.84 kJ·mol^{-1}) is not small enough for the entropy effect to be the dominant term. This means that the formation of ordered intermetallic compounds with solid solution are expected to form [19].

3.3. First Hydrogenation Properties

Figure 4 shows the first hydrogenation (activation) curve of the as-cast alloy. The activation was performed at room temperature under a hydrogen pressure of 20 bars without any prior treatment.

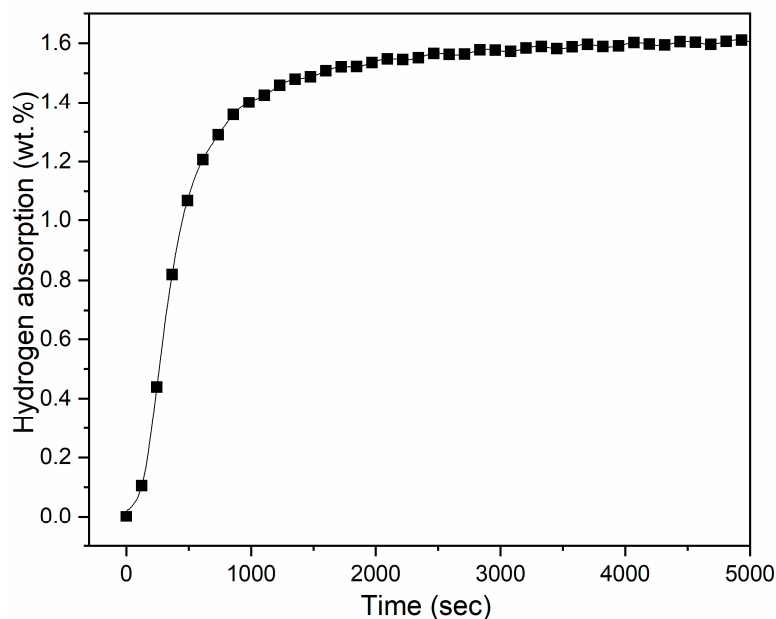**Figure 4.** Activation curve of as-cast $Ti_{0.3}V_{0.3}Mn_{0.2}Fe_{0.1}Ni_{0.1}$ alloy.

The alloy absorbs hydrogen, reaching a maximum capacity of 1.6 wt.% within one hour. Even if the alloy is multiphase, the activation curve seems to behave as a single-phase absorption.

In an attempt to find the crystal structure of the hydride alloy, the experiment was stopped after reaching full hydrogenation and the powder immediately prepared for X-ray diffraction. The result is presented in Figure 5. The crystal parameters and abundance of each phase as determined by Rietveld's refinement are shown in Table 4.
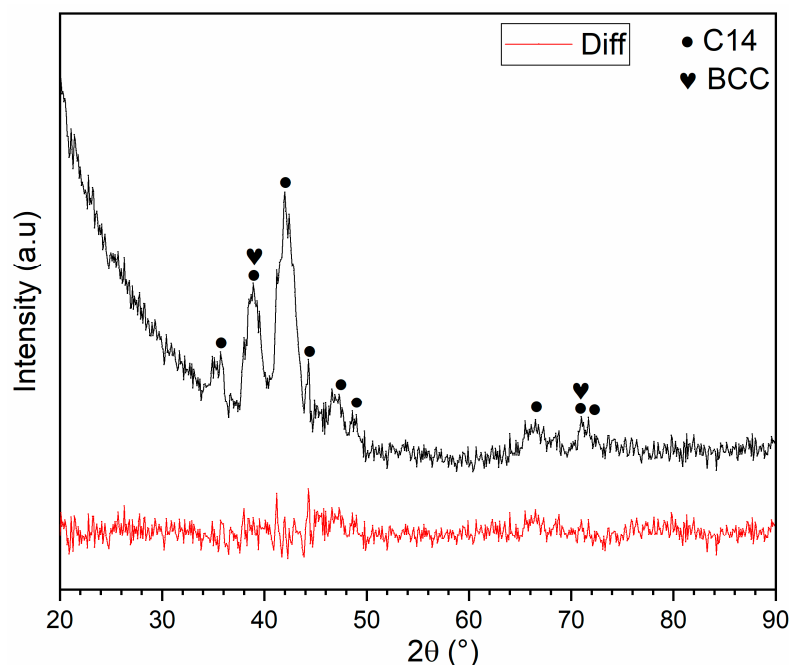

Figure 5. XRD patterns of the hydride sample.

Table 4. Crystal structure parameters and abundance of each phase in the hydride sample. Error on the last significant digit is indicated in parentheses.

Phase	Unit Cell Volume Å^3	Lattice Parameter Å	Crystallite Size nm	Micro-Strain %	Abundance %
C14	187.85 (9)	a = 5.1091 (1) c = 8.2835 (2)	11 (3)	0.62 (3)	92
BCC	34.5 (2)	3.257 (6)	7 (2)	———	8

Compared to the as-cast sample, the abundance of C14 increased from 79% to 92%, while the abundance of BCC phase decreased from 17% to 8%. There was no evidence of Ti_2Fe like phase in the hydride pattern. From the lattice expansion of each phase and assuming that the volume taken by a hydrogen atom is 2.9 Å^3 [35], the amount of hydrogen in each hydride phase could be estimated. Table 5 presents the volume expansion of the hydride phases with the estimated value of hydrogen per metallic atom (H/M) and corresponding wt.%. We see that, for the C14 phase, the H/M ratio is 2.0, which corresponds to the dihydride. In the case of the BCC phase, the H/M is 1.4. It is known that upon hydrogenation a BCC phase adopts a BCT (body centered tetragonal) structure for the monohydride and an FCC (face centered cubic) dihydride. It is therefore strange that, in the present case, the BCC phase absorbed up to H/M 1.4 but still maintained the BCC structure. However, it has been shown that for the HEA TiVZrHfNb [12,13] and TiVZrNbHf-based HEAs the BCT structure could have a H/M of 2. In the present case, the crystal structure is indexed to a BCC, but the broadness of the peaks and the overlap with C14 peaks makes it difficult to clearly distinguish between a BCC and BCT structure.

Table 5. Estimated capacity of the phases in the hydrided sample.

Phase	Volume Expansion (Å^3)	H/M	Estimated Capacity of the Phase (wt.%)
C14	22.9	2.0	1.2
BCC	7.9	1.4	2.6

From Table 5 and taking into consideration the abundance of each phase, the estimated amount of hydrogen in the hydride sample is about 1.3 wt.%. This is relatively far from the measured capacity of 1.6 wt.%. However, as the pattern was taken at room temperature and in air, there is a possibility that some desorption occurred. Therefore, we can not be absolutely certain that the pattern shown in Figure 5 is for a fully hydride sample. However, this is an indication that the hydride phase is probably very stable at room temperature.

3.4. Air Exposure Effect

It is easier to handle the alloy in the air rather than in argon atmosphere. This stimulated us to study the air exposure effect on the as-cast $Ti_{0.3}V_{0.3}Mn_{0.2}Fe_{0.1}Ni_{0.1}$ alloy. Figure 6 shows the activation curves of the crushed alloy crushed under argon and in air. After crushing in air, the sample was also further exposed to the air for two and five days.
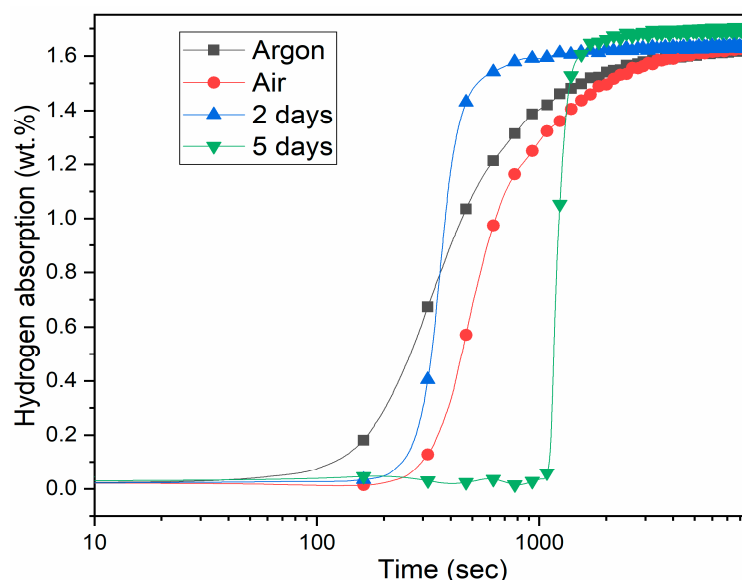

Figure 6. Activation curves at room temperature under 20 bars of hydrogen of as-cast $Ti_{0.3}V_{0.3}Mn_{0.2}Fe_{0.1}Ni_{0.1}$ alloy crushed in argon and air. The sample crushed in air was further exposed for two and five days.

The sample crushed in argon has 40 s incubation time while the one crushed in air needed 200 s before absorbing hydrogen. However, the intrinsic kinetic (tangent at mid capacity) was the same for the samples crushed in air or argon. Surprisingly, two days of air exposure did not change the incubation time but the intrinsic kinetic was about four times faster than the sample simply crushed in air. The sample exposed for five days has the longest incubation time of 1080 s. The intrinsic kinetic was slower than the two-day air exposed but still about three times faster than the air crushed sample. This long incubation time is probably related to the thick oxide layer caused by the long exposure to air. We have seen from the TiFe alloy that the presence of some level of oxide could speed up the intrinsic kinetics of hydrogenation [36]. The faster intrinsic kinetic of the air exposed samples may be due to the catalytic effect of the TiO_2 layer on the surface. However, this has to be confirmed in a dedicated investigation. It should be noted that air exposure did not reduce the hydrogen capacity.

3.5. Synthesis by Mechanical Alloying

The $Ti_{0.3}V_{0.3}Mn_{0.2}Fe_{0.1}Ni_{0.1}$ alloy was also synthesized by mechanical alloying. To synthesize the alloy, the raw materials Ti, V, Mn, Fe and Ni were mixed in the desired proportion and milled for 1, 5, and 10 h. Figure 7 presents the evolution of XRD patterns of the milled powder.
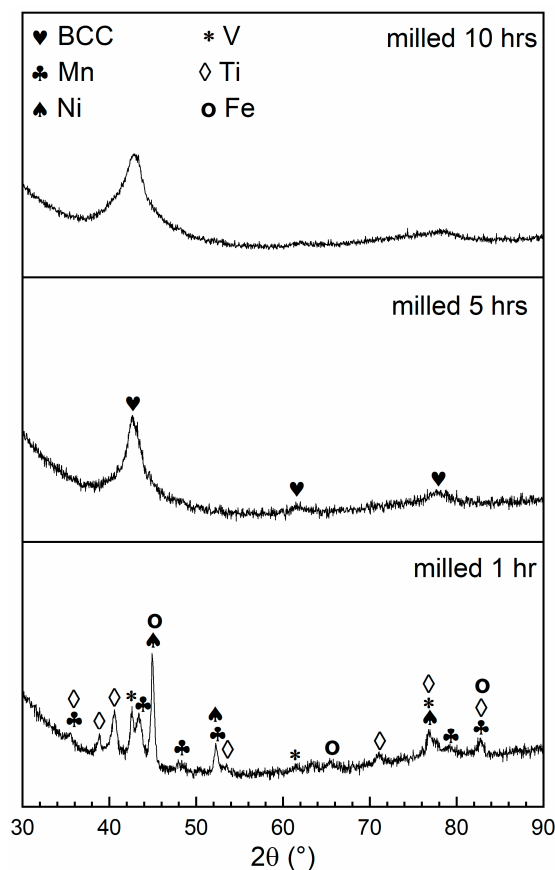
Figure 7. XRD patterns of Ti-V-Mn-Fe-Ni powders milled for 1, 5, and 10 h.

After one hour of milling, the Bragg peaks from all raw elements are still present. The five-hour milled pattern shows the formation of a BCC phase. Milling for 10 h leads to further broadening of the BCC peaks. The diffraction patterns were analyzed by Rietveld's refinement and the obtained crystal parameters of the BCC phase are shown in Table 6.

Table 6. Crystal parameters of the BCC phase of the samples milled for 5 and 10 h. Error on the last significant digit is indicated in parentheses.

Milling Time (hr)	Unit Cell Volume ($Å^3$)	Lattice Parameter (Å)	Crystallite Size (nm)
5	28.0 (2)	3.035 (6)	2.30 (5)
10	27.7 (4)	3.03 (1)	1.40 (2)

We see that after the formation of a BCC phase, further milling essentially reduces the crystallite size. Actually, such a small crystallite size means that the structure is very close to amorphous. For this reason, the first hydrogenation tests were done on the sample milled for five hours as this sample is most likely to have a true BCC structure. It should be noted that the lattice parameter of the BCC phase of the ball milled sample is bigger than the BCC phase of the as-cast alloy by around 1.7%. This may be explained by the fact that the milled BCC has the exact nominal composition while the BCC formed by arc melting

is slightly depleted in vanadium (the biggest atomic radius) and enriched in nickel (the smallest atomic radius).

3.6. Effect of Milling on As-Cast Alloy

We investigated the effect of ball milling for 1, 5, and 10 h on as-cast $Ti_{0.3}V_{0.3}Mn_{0.2}Fe_{0.1}Ni_{0.1}$ alloy. The X-ray patterns are shown in Figure 8.
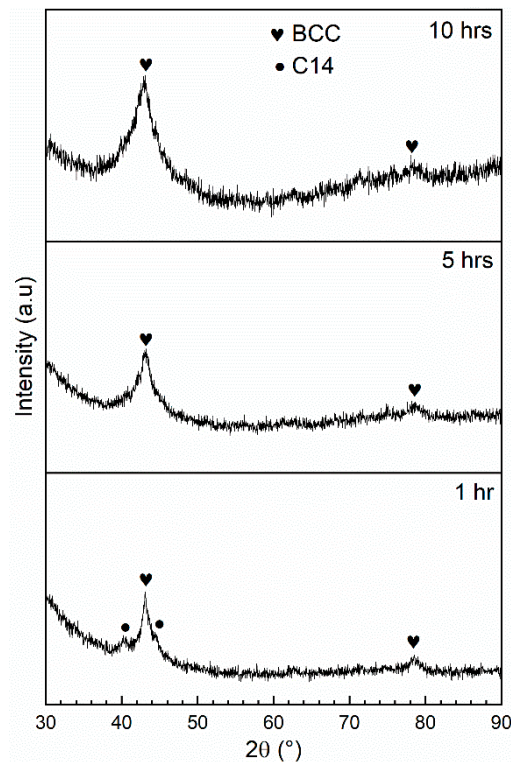
Figure 8. X-ray diffraction patterns of as-cast $Ti_{0.3}V_{0.3}Mn_{0.2}Fe_{0.1}Ni_{0.1}$ alloy before and after milling for 1, 5, and 10 h.

Before milling, the $Ti_{0.3}V_{0.3}Mn_{0.2}Fe_{0.1}Ni_{0.1}$ alloy was multiphase with C14, BCC, and Ti_2Fe-type phases. After milling for one hour, the crystal structure was mainly BCC with some C14 phase. The peaks of the Ti_2Fe type phase could not be identified. After five hours of milling, only broad BCC peaks were present. A similar result was obtained by Amira et al. who studied the effect of ball milling on cast $TiCr_x$ alloys. They found that $TiCr_x$ transforms from a mixture of C14 and C15 Laves phases to a metastable BCC phase after milling five hours under argon [37]. In the present case, as expected, further milling to 10 h had the effect of decreasing the crystallite size and thus broadening the Bragg's peaks of the BCC phase. Additionally, the Bragg's BCC peak is shifted to lower angles with milling time. This is an indication of the increasing lattice parameter of the BCC phase. Table 7 lists the crystal structure parameters and the abundance of each phase in the cast alloy before and after milling as given by Rietveld's refinement.

In the case of C14 phase, milling up to 1 h does not significantly change the lattice parameters and the unit cell volume but it causes an important decrease in the crystallite size. For the BCC phase, with milling the lattice parameter increases and the crystallite size is reduced to approximately one nanometer after 10 h.

Milling the cast alloy produced similar results to milling the raw elements. As in the case of milling the raw elements, we selected the five-hour-milled sample to perform the hydrogenation test.

Table 7. Crystal parameters and abundance of each phase in as-cast $Ti_{0.3}V_{0.3}Mn_{0.2}Fe_{0.1}Ni_{0.1}$ alloy before and after milling. Error on the last significant digit is indicated in parentheses.

Milling Time (hr)	Phase	Unit Cell Volume ($Å^3$)	Lattice Parameter (Å)	Crystallite Size (nm)	Abundance (%)
0	C14	164.98 (3)	a = 4.8900 (4) c = 7.9651 (9)	125 (48)	79
	BCC	26.58 (1)	2.9841 (5)	31 (5)	17
	Ti_2Fe	1418 (3)	11.234 (8)	——	4
1	C14	165.9 (6)	4.897 (7) 7.989 (2)	13.0 (2)	36
	BCC	27.02 (1)	3.001 (4)	4.0 (2)	64
5	BCC	27.60 (4)	3.02 (1)	1.88 (6)	100
10	BCC	28.60 (4)	3.06 (1)	1.12 (3)	100

3.7. First Hydrogenation of the Milled Raw Powder and the Alloy

The first hydrogenation of both samples formed after five hours of milling is shown in Figure 9 and compared to the as-cast alloy. The measurements were performed at room temperature under a hydrogen pressure of 20 bars without any prior treatment.
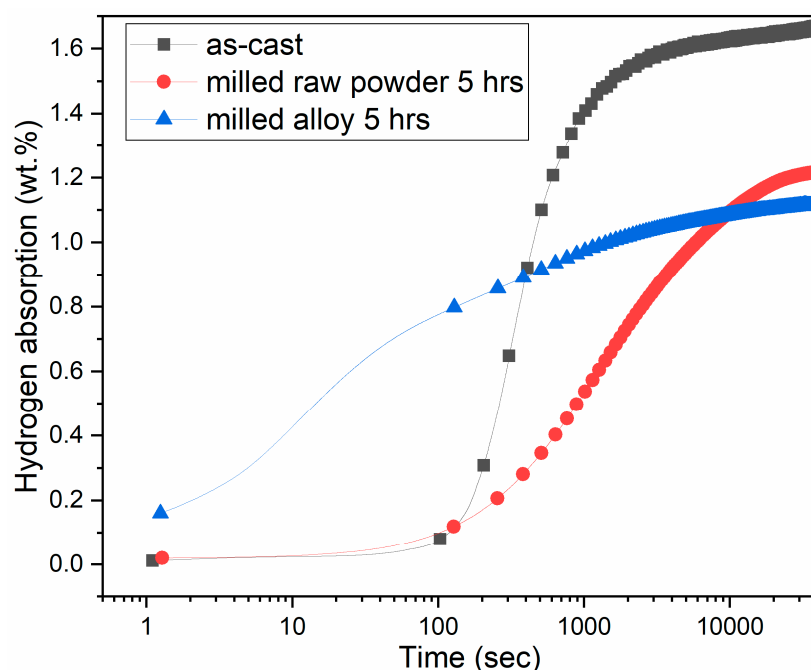

Figure 9. Activation curves of the milled raw powder for five hours, the as-cast alloy further milled for five hours, and the as-cast one.

The milled raw powder and the as-cast alloy have the same incubation time. The maximum capacity reached by the milled raw powder sample is 1.2 wt.% H, which is lower than the capacity of the as-cast alloy (1.6 wt.%). The reduction in capacity is most likely due to the reduction in crystallite size. Assuming that the grain boundaries are just one unit cell thick, the grain boundary volume for the five-hour ball milled materials is almost 50%. This grain boundary most probably does not store hydrogen at the same level as the BCC phase. Therefore, the total capacity is severely lowered. The same effect was seen for the TiFe alloy [38].

The milled alloy readily absorbs hydrogen without incubation time. In our apparatus, the first second of absorption is not recorded. Additionally, we see an initial capacity of 0.16 wt.%, therefore we assume that the real capacity of the milled alloy should be increased

by about 0.1 wt.%. Therefore, the total capacity of this alloy is probably around 1.2 wt.%, which is the same capacity obtained by milling the raw elements for five hours. Figure 10 shows the XRD patterns of the hydrogenated alloys after full hydrogenation.
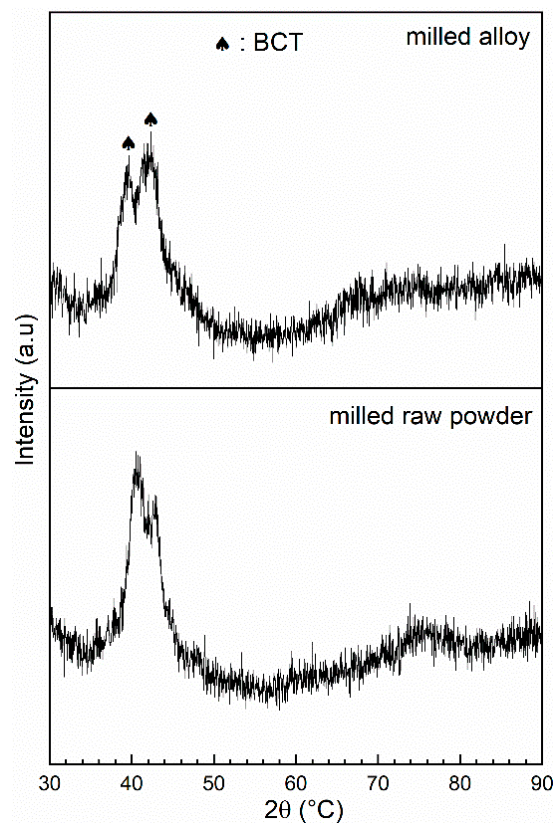
Figure 10. XRD patterns of the milled raw powder and milled alloy in the hydrogenated state.

Upon hydrogenation, the crystal structure of both samples is BCT of space group I4/mmm. It was shown by Nakamura and Akiba that the monohydride of the BCC phase has a BCT (body centered tetragonal) structure [39]. The transformation into BCT instead of the dihydride FCC could be because of a high hysteresis. From Rietveld's analysis, the crystal structure parameters of the BCT phase for milling the raw materials are the same as for the milled alloy. The unit cell volume is 30.1 (5) $Å^3$, a = 2.99 (2) Å and c = 3.36 (3) Å. The crystallite size is 1.51 (5) nm. The c/a ratio of the BCT phase is 1.12, which is in agreement with cases where the distortion of the lattice caused by hydrogen is along the c-axis [40]. Taking into account that each hydrogen atom occupies a volume of 2.9 $Å^3$, we could estimate that the BCC phase in the hydrogenated state has a capacity of around 0.7 wt.%, which is smaller than the measured capacity of 1.2 wt.%. However, as indicated above, because the X-ray diffraction was under air, there is a likelihood that the sample partially desorbed.

4. Conclusions

The alloy $Ti_{0.3}V_{0.3}Mn_{0.2}Fe_{0.1}Ni_{0.1}$ was successfully synthesized by arc-melting and mechanical alloying. The arc-melted alloy has a multiphase structure, with a main C14 Laves phase matrix along with a BCC phase and a small amount of Ti_2Fe-type phase. Its maximum hydrogen storage capacity was 1.6 wt.%. Upon hydrogenation, the Ti_2Fe-type phase disappeared. The initial C14 and BCC phases were converted into the C14 and BCC hydrides, respectively. The H/M value was 1.4 in the hydride BCC. Air exposure for two or five days has no impact on the hydrogen capacity but changed the kinetics.

Synthesis by mechanical alloying for five hours resulted in an alloy with BCC structure. The hydrogen capacity of the milled alloy was lower than the as-cast one. The BCC structure

transforms after hydrogen absorption (under 20 bars of H_2) to monohydride phase "BCT" and not to dihydride "FCC". The effect of ball milling of the as-cast alloy was also studied. Ball milling for five hours produced a BCC structure similar to the one obtained by milling the raw elements for five hours. The first hydrogenation measurements showed that milling for five hours leads to a faster kinetics compared to the as-cast sample but with a reduced capacity. The synthesis of $Ti_{0.3}V_{0.3}Mn_{0.2}Fe_{0.1}Ni_{0.1}$ by arc-melting is better than by mechanical alloying because arc-melted alloy shows a higher capacity.

Author Contributions: All experiments, except electron microscopy, were performed by S.S. and M.M. under the supervision of J.H. J.H. and S.S. analyzed the results and wrote the paper. All authors have read and agreed to the published version of the manuscript.

Conflicts of Interest: The authors declare no conflict of interest.

References

1. Anstrom, J. Hydrogen as a fuel in transportation. In *Advances in Hydrogen Production, Storage and Distribution*; Basile, A., Lulianelli, A., Eds.; Elsevier: Amsterdam, The Netherlands, 2014; pp. 499–524.
2. Schlapbach, L.; Züttel, A. Hydrogen-storage materials for mobile applications. In *Materials for Sustainable Energy*; Co-Published with Macmillan Publishers Ltd.: London, UK, 2012; pp. 265–270. [CrossRef]
3. Züttel, A.; Remhof, A.; Borgschulte, A.; Friedrichs, O. Hydrogen: The future energy carrier. *Philos. Trans. R. Soc. Lond. A Math. Phys. Eng. Sci.* **2010**, *368*, 3329–3342. [CrossRef] [PubMed]
4. Reilly, J. Metal hydride technology. *Z. Für Phys. Chem.* **1979**, *117*, 155–184. [CrossRef]
5. Cantor, B.; Chang, I.; Knight, P.; Vincent, A. Microstructural development in equiatomic multicomponent alloys. *Mater. Sci. Eng. A* **2004**, *375*, 213–218. [CrossRef]
6. Yeh, J.W.; Chen, S.K.; Lin, S.J.; Gan, J.Y.; Chin, T.S.; Shun, T.T.; Tsau, C.H.; Chang, S.Y. Nanostructured high-entropy alloys with multiple principal elements: Novel alloy design concepts and outcomes. *Adv. Eng. Mater.* **2004**, *6*, 299–303. [CrossRef]
7. Gao, M.C.; Yeh, J.-W.; Liaw, P.K.; Zhang, Y. *High-Entropy Alloys: Fundamentals and Applications*; Springer: Berlin/Heidelberg, Germany, 2016.
8. Zhang, W.; Liaw, P.K.; Zhang, Y. Science and technology in high-entropy alloys. *Sci. China Mater.* **2018**, *61*, 1–21. [CrossRef]
9. Kunce, I.; Polanski, M.; Bystrzycki, J. Structure and hydrogen storage properties of a high entropy ZrTiVCrFeNi alloy synthesized using Laser Engineered Net Shaping (LENS). *Int. J. Hydrogen Energy* **2013**, *38*, 12180–12189. [CrossRef]
10. Kunce, I.; Polanski, M.; Bystrzycki, J. Microstructure and hydrogen storage properties of a TiZrNbMoV high entropy alloy synthesized using Laser Engineered Net Shaping (LENS). *Int. J. Hydrogen Energy* **2014**, *39*, 9904–9910. [CrossRef]
11. Kunce, I.; Polański, M.; Czujko, T. Microstructures and hydrogen storage properties of LaNiFeVMn alloys. *Int. J. Hydrogen Energy* **2017**, *42*, 27154–27164. [CrossRef]
12. Sahlberg, M.; Karlsson, D.; Zlotea, C.; Jansson, U. Superior hydrogen storage in high entropy alloys. *Sci. Rep.* **2016**, *6*, 36770. [CrossRef]
13. Karlsson, D.; Ek, G.; Cedervall, J.; Zlotea, C.; Møller, K.T.; Hansen, T.C.; Bednarcik, J.; Paskevicius, M.; Sørby, M.H.; Jensen, T.R. Structure and hydrogenation properties of a HfNbTiVZr high-entropy alloy. *Inorg. Chem.* **2018**, *57*, 2103–2110. [CrossRef]
14. Kao, Y.-F.; Chen, S.-K.; Sheu, J.-H.; Lin, J.-T.; Lin, W.-E.; Yeh, J.-W.; Lin, S.-J.; Liou, T.-H.; Wang, C.-W. Hydrogen storage properties of multi-principal-component CoFeMnTixVyZrz alloys. *Int. J. Hydrogen Energy* **2010**, *35*, 9046–9059. [CrossRef]
15. Zepon, G.; Leiva, D.; Strozi, R.; Bedoch, A.; Figueroa, S.; Ishikawa, T.; Botta, W. Hydrogen-induced phase transition of MgZrTiFe 0.5 Co 0.5 Ni 0.5 high entropy alloy. *Int. J. Hydrogen Energy* **2018**, *43*, 1702–1708. [CrossRef]
16. Zhang, Y.; Zhou, Y.J.; Lin, J.P.; Chen, G.L.; Liaw, P.K. Solid-solution phase formation rules for multi-component alloys. *Adv. Eng. Mater.* **2008**, *10*, 534–538. [CrossRef]
17. Takeuchi, A.; Inoue, A. Classification of Bulk Metallic Glasses by Atomic Size Difference, Heat of Mixing and Period of Constituent Elements and Its Application to Characterization of the Main Alloying Element. *Mater. Trans.* **2005**, *46*, 2817–2829. [CrossRef]
18. Yang, X.; Zhang, Y. Prediction of high-entropy stabilized solid-solution in multi-component alloys. *Mater. Chem. Phys.* **2012**, *132*, 233–238. [CrossRef]
19. Zhang, Y.; Lu, Z.; Ma, S.; Liaw, P.; Tang, Z.; Cheng, Y.; Gao, M. Guidelines in predicting phase formation of high-entropy alloys. *Mrs Commun.* **2014**, *4*, 57–62. [CrossRef]
20. Guo, S.; Ng, C.; Lu, J.; Liu, C. Effect of valence electron concentration on stability of fcc or bcc phase in high entropy alloys. *J. Appl. Phys.* **2011**, *109*, 103505. [CrossRef]
21. Elements, Atomic Radii and the Periodic Table. Available online: http://www.crystalmaker.com/support/tutorials/atomic-radii/ (accessed on 12 February 2021).

22. Ptable. Available online: https://www.ptable.com/ (accessed on 12 February 2021).
23. Bruker, A. Topas V3: General profile and structure analysis software for powder diffraction data–user's manual. In *Coelho Software*; TOPAS Academic: Brisbane, Australia, 2005.
24. Collins, T.J. ImageJ for microscopy. *Biotechniques* **2007**, *43*, 25–30. [CrossRef] [PubMed]
25. Deying, S.; Xueping, G.; Yunshi, Z.; Jie, Y.; Panwen, S. Characteristics of titanium-based C14-type Laves phase alloys and their hydride electrodes. *J. Alloys Compd.* **1994**, *206*, 43–46. [CrossRef]
26. Challet, S.; Latroche, M.; Heurtaux, F. Hydrogenation properties and crystal structure of the single BCC (Ti0. 355V0. 645) 100−xMx alloys with M = Mn, Fe, Co, Ni (x = 7, 14 and 21). *J. Alloys Compd.* **2007**, *439*, 294–301. [CrossRef]
27. Couillaud, S.; Enoki, H.; Amira, S.; Bobet, J.-L.; Akiba, E.; Huot, J. Effect of ball milling and cold rolling on hydrogen storage properties of nanocrystalline TiV1.6Mn0.4 alloy. *J. Alloys Compd.* **2009**, *484*, 154–158. [CrossRef]
28. Aleksanyan, A.; Dolukhanyan, S.; Ter-Galstyan, O.; Mnatsakanyan, N. Hydride cycle formation of ternary alloys in TiVMn system and their interaction with hydrogen. *Int. J. Hydrogen Energy* **2016**, *41*, 13521–13530. [CrossRef]
29. Huang, T.; Wu, Z.; Sun, G.; Xu, N. Microstructure and hydrogen storage characteristics of TiMn2−XVX alloys. *Intermetallics* **2007**, *15*, 593–598. [CrossRef]
30. Nakamura, Y.; Nakamura, J.; Sakaki, K.; Asano, K.; Akiba, E. Hydrogenation properties of Ti–V–Mn alloys with a BCC structure containing high and low oxygen concentrations. *J. Alloys Compd.* **2011**, *509*, 1841–1847. [CrossRef]
31. Bibienne, T.; Tousignant, M.; Bobet, J.-L.; Huot, J. Synthesis and hydrogen sorption properties of TiV (2−x) Mnx BCC alloys. *J. Alloys Compd.* **2015**, *624*, 247–250. [CrossRef]
32. Huot, J.; Enoki, H.; Akiba, E. Synthesis, phase transformation, and hydrogen storage properties of ball-milled TiV0. 9Mn1. 1. *J. Alloys Compd.* **2008**, *453*, 203–209. [CrossRef]
33. Huot, J.; Akiba, E.; Ishido, Y. Crystal structure of multiphase alloys (zr, ti)(mn, v) 2. *J. Alloys Compd.* **1995**, *231*, 85–89. [CrossRef]
34. Huot, J.; Akiba, E.; Iba, H. Crystal structure and phase composition of alloys $Zr_{1-x}Ti_x(Mn_{1-y}V_y)_2$. *J. Alloys Compd.* **1995**, *228*, 181–187. [CrossRef]
35. Peisl, H. Lattice strains due to hydrogen in metals. In *Hydrogen in Metals I*; Springer: Berlin/Heidelberg, Germany, 1978; pp. 53–74.
36. Gosselin, C.; Huot, J. Hydrogenation properties of tife doped with zirconium. *Materials* **2015**, *8*, 7864–7872. [CrossRef]
37. Amira, S.; Santos, S.; Huot, J. Hydrogen sorption properties of Ti–Cr alloys synthesized by ball milling and cold rolling. *Intermetallics* **2010**, *18*, 140–144. [CrossRef]
38. Lv, P.; Guzik, M.N.; Sartori, S.; Huot, J. Effect of ball milling and cryomilling on the microstructure and first hydrogenation properties of tife+ 4 wt.% zr alloy. *J. Mater. Res. Technol.* **2019**, *8*, 1828–1834. [CrossRef]
39. Nakamura, Y.; Akiba, E. Hydriding properties and crystal structure of nacl-type mono-hydrides formed from ti–v–mn bcc solid solutions. *J. Alloys Compd.* **2002**, *345*, 175–182. [CrossRef]
40. Fukai, Y. *The Metal-Hydrogen System: Basic Bulk Properties*; Springer Science & Business Media: Berlin/Heidelberg, Germany, 2006; Volume 21.